Applied Energy 357 (2024) 122477

Contents lists available at ScienceDirect

Applied Energy

journal homepage: www.elsevier.com/locate/apenergy

Modeling and optimal operation of reversible solid oxide cells considering heat recovery and mode switching dynamics in microgrids

Chunjun Huang [a], Goran Strbac [b], Yi Zong [a,*], Shi You [a], Chresten Træholt [a], Nigel Brandon [b], Jiawei Wang [b,c], Hossein Ameli [b]

[a] Department of Wind and Energy Systems, Technical University of Denmark, 2800 Kgs. Lyngby, Denmark
[b] Imperial College London, South Kensington, London SW7 2BU, United Kingdom
[c] Northumbria University, Newcastle-upon-Tyne NE1 8ST, United Kingdom

ARTICLE INFO

Keywords:
Reversible solid oxide cells
Heat recovery
Optimal operation of microgrids
Power-to-hydrogen
Multi-energy management

ABSTRACT

The reversible solid oxide cell (rSOC) is a promising technology for advancing energy decarbonization by enabling bidirectional conversion between electricity and hydrogen in a single device. However, previous studies have not fully explored the operational flexibility of rSOCs due to inadequate consideration of heat recovery potentials and dynamics of operating mode transitions. To address this research gap, this paper presents a model-based optimal operation method for managing multi-energy transactions in rSOC-based microgrids, aiming to minimize operation costs. The method incorporates detailed operational models of the rSOC, including a lumped thermal model to account for heat recovery capability and modeling of various operating modes and their transitions. Additionally, a linearization process is introduced to address nonlinear and implicit operational constraints, resulting in a computationally efficient mixed-integer linear programming (MILP) formulation for the operation model. Comparative case studies are conducted using modified energy portfolios of a Danish energy island. The results demonstrate that the proposed method effectively captures operating mode transitions within the rSOC and enhances its profitability via waste heat recovery. Notably, the rSOC model contributes to enhanced operational flexibility through heat recovery behaviors and a wider temperature range, resulting in substantial economic savings for the microgrid.

1. Introduction

The global imperative to mitigate environmental concerns, particularly climate change, has necessitated a rapid shift from fossil fuel usage towards sustainable and green energy sources. In this context, renewable energy sources (RESs), such as wind and solar energy, have emerged as highly promising and efficient solutions for facilitating the ongoing energy transition. Notably, the European Union has set forth a comprehensive target of achieving a minimum RES integration of 42.5% by 2030, with the overarching objective of reducing greenhouse gas emissions by at least 55% [1]. Furthermore, the International Renewable Energy Agency (IRENA) has articulated an ambitious vision wherein RESs are projected to contribute to 85% of the power sector, thereby advancing the critical agenda of energy decarbonization [2]. These collective targets underscore the anticipated trajectory wherein RESs are poised to increasingly dominate and be seamlessly integrated into the fabric of green energy systems.

However, the intermittent and fluctuating nature of RESs presents significant challenges to the stability and reliability of energy systems. Energy storage devices, such as batteries, supercapacitors, and pumped hydro, have been widely acknowledged as viable solutions to mitigate the adverse effects of RESs [3]. As a clean energy storage medium, hydrogen has emerged as a promising green alternative for energy storage, particularly for long-term (e.g. seasonal periods) and large-scale energy storage [4]. Based on water electrolysis technologies such as alkaline electrolyzers, proton exchange membrane electrolyzers, and solid oxide electrolysis cell (SOEC) [5], surplus power produced from RESs can be efficiently converted into hydrogen and stored. Moreover, the stored hydrogen can be reconverted into electricity to meet required electrical demands via fuel cell technologies e.g. solid oxide fuel cell (SOFC) [6]. Thus, integrating hydrogen-related technologies with RESs offers a decarbonized and green solution to handle the barrier of RESs integration, while providing operational flexibility to support stability and reliability in renewable energy systems [7].

Among these hydrogen-related technologies, the reversible solid oxide cell (rSOC) which combines the functionalities of SOECs and SOFCs within a single device, possesses advantages such as reduced footprint,

* Corresponding author.
E-mail addresses: chunhua@dtu.dk (C. Huang), g.strbac@imperial.ac.uk (G. Strbac), yizo@dtu.dk (Y. Zong).

https://doi.org/10.1016/j.apenergy.2023.122477
Received 22 August 2023; Received in revised form 26 October 2023; Accepted 5 December 2023
Available online 20 December 2023

Nomenclature

Abbreviation

BOP	Balance of plant
CHP	Combined heat and power
DER	Distributed energy resource
ECED	Endothermic electrolysis mode
ECEX	Exothermic electrolysis mode
EC	Electrolysis mode
HES	Hydrogen energy system
MFC	Mass flow controller
MILP	Mixed-integer linear programming
rSOC	Reversible solid oxide cell
SOEC	Solid oxide electrolysis cell
SOFC	Solid oxide fuel cell
Superscript t	Time instant t
TEC	Transition from FC to EC
TFC	Transition from EC to FC

Parameters

$\dot{T}_{max}$	Maximum temperature gradient (K/min)
a_i, b_i	Coefficients in calculating the rSOC's efficiency
C_{cur}	Penalty cost for wind curtailment (€/MWh)
$C_{ele}, C_{heat}, C_{H_2}$	Electricity price (€/MWh), heat price (€/MWh), and hydrogen price (€/kg)
C_{rSOC}^{lump}	Heat capacitance of the rSOC system (MWh/°C)
E_b, E_{H_2}	Rated capacity of battery and hydrogen tank (kWh)
k_i	Coefficients in the expression of heat loss
l	Thickness of the insulation (m)
L_b^{min}, L_b^{max}	Minimum/maximum capacity of battery (%)
$L_{H_2}^{min}, L_{H_2}^{max}$	Minimum/maximum capacity of hydrogen tank (%)
LHV	Lower heat value of hydrogen (kWh/kg)
M, δ	Constants for model linearization
n	Number of cells within one stack
$P_{ch}^{min}, P_{ch}^{max}$	Minimum and maximum charging power of battery (kW)
$P_{cur}^{min}, P_{cur}^{max}$	Minimum and maximum renewable power curtailed (kW)
$P_{dis}^{min}, P_{dis}^{max}$	Minimum and maximum discharging power of battery (kW)
$P_{ec}^{min}, P_{ec}^{max}$	Minimum and maximum power in EC mode (kW)
$P_{fc}^{min}, P_{fc}^{max}$	Minimum and maximum power in FC mode (kW)
$P_{grid}^{min}, P_{grid}^{max}$	Minimum and maximum purchased power from power grids (kW)
$P_{res}, P_{chp}, P_{load}$	Renewable power production, CH's power production,load consumptions (kW)
P_{tec}^N, P_{tfc}^N	Power demand in TEC and TFC mode (kW)
T_s	Time resolution (h)
V_{rSOC}	Volume of the rSOC system (m^3)

Variables

$\mathcal{W}, \mathcal{W}_{1,2,3}, \mathcal{H}, \mathcal{F}_{1,2}$	Intermediate variables for model linearization
$\omega, \lambda, h^u, h^l$	Auxiliary variables in the piece-wise linearization method
$\delta_{dis}, \delta_{ch}$	Binary variable for enabling battery to discharge and charge
$\delta_{grid}, \delta_{cur}$	Binary variable for enabling purchased power and curtailed power
$\dot{m}_{H_2}$	Hydrogen sold (kg/h)
η_{fc}, η_{ec}	Efficiency of rSOC at FC and EC mode
$\delta_{fc}, \delta_{ecex}, \delta_{eced}, \delta_{tec}, \delta_{tfc}$	Binary variable for enabling different operation modes of rSOC
L_b, L_{H_2}	Capacity level of battery and hydrogen tank (%)
P_{ch}, P_{dis}	Battery's charging and discharging power of battery (kW)
P_{cur}	Renewable power curtailed (kW)
$P_{fc}, P_{ec}, P_{tfc}, P_{tec}$	rSOC power at FC, EC, TFC, TEC mode (kW)
P_{grid}	Purchased power from power grid (kW)
P_{rSOC}	Consumed power of rSOC (kW)
Q_e	Heat generated of rSOC(kW)
Q_{loss}	Heat loss to the environment (kW)
Q_{rec}	Heat recovered of AEL stack (kW)
T_c	The temperature of the cold face of the insulation within rSOC (K)
T_{rSOC}	Operating temperature of rSOC (K)

compact structure, and higher round-trip efficiency, making them a potentially efficient method for accommodating RESs reliably [8]. In [9], the authors develop a sizing procedure for isolated microgrids based on rSOCs to determine the optimal capacities of RESs and storage systems. The rSOC system converts the surplus renewable power into hydrogen (electrolysis mode) or consumes hydrogen to generate electricity (fuel cell mode) compensating for the deficit power, thereby maintaining the reliable supply for demands. Hydrogen and thermal storage systems are employed for energy buffering, facilitating the storage of produced hydrogen during electrolysis mode and utilizing released heat during fuel cell mode. In particular, the stored heat can provide the required heat for the rSOC working at the endothermic electrolysis mode. Building upon this work, the authors extend the scope to a grid-connected microgrid incorporating rSOCs [10]. They propose a dynamic programming framework for optimal sizing and control of the rSOC unit, aiming to achieve optimal energy management between the rSOC and external grids. This approach reduces the installed power requirements of the rSOC and shortens the payback period. Furthermore, Ref. [11] improves improve upon the dynamic programming approach by introducing a dual-state control strategy. Unlike the single-state control only related to hydrogen storage in [10], this improved control simultaneously considers variations in both hydrogen and thermal storage states, effectively integrating thermal power management into microgrid optimization. The authors in [12] also investigate the sizing of microgrids integrated with rSOCs only and hybrid rSOCs and batteries. The economic performance of allocating different energy storage solutions is compared. In particular, detailed technical constraints of rSOCs are considered in the sizing model including their ramping capability and partial-load range.

However, the aforementioned studies rarely have paid limited attention to the mode switching process of rSOCs in their operation, primarily due to the assumption of hour-level time resolution in previous studies. However, given that mode switching process will occur

Table 1
Comparisons between current studies and our work.

Research	Optimal operation in microgrids	Mode switching process	Energy conversion among electricity, hydrogen and heat	Heat recovery potentials
[9–11]	√	×	Fitted mathematical models	Partly (only recovered thermal power at fuel cell mode)
[12]	√	×	Only between electricity and hydrogen	×
[13]	×	√	×	×
[14]	√	√	Only between electricity and hydrogen	×
[15–17]	×	√	× (high-order dynamic models of rSOC)	×
Our work	√	√	√ (physical-based models)	√[a]

[a] A thermal model is developed for evaluating the heat recovered at different modes, and the revenue of heat recovered is integrated into the operation model.

within shorter time intervals, such as 2.5–15 min [13,14], capturing the switching transients and their effects becomes crucial for the operation with minute-level resolution. Meanwhile, These transients involve diverse electrical and thermal characteristics, including power output, temperature variation, and efficiency [15], which need to be integrated into the operational strategy to ensure reliable rSOC operation. Some researchers have developed validated dynamic models of rSOCs based on experimental data to capture the transient behavior during mode switching [15], and examine the impact of rSOC system parameters on the thermal characteristics [16]. Thermal management strategies have also been proposed to mitigate temperature fluctuations during mode switching, considering thermochemical energy storage and utilizing 2-dimensional non-adiabatic dynamic models [17]. However, these studies have limited references to the mode switching process from the perspective of rSOC operation. Moreover, their complex models pose challenges for direct integration into optimal operation and sizing models of rSOC-based microgrids due to computational burden. Nevertheless, Ref. [14] presents a valuable reference on integrating mode switch dynamics into the optimal energy management of rSOC-based renewable communities, incorporating constraints of switching sequences between transient and steady-state modes of rSOCs with a 15-min time resolution.

Table 1 provides an overview of previous studies on the operation of rSOCs. However, several research gaps can be identified. Firstly, current studies have quite limited consideration for the mode switching process of rSOCs when implementing system-level operation for microgrids, as [9–12]. Although several publications [15–17] focused on building detailed dynamic models to characterize the transient performance of rSOCs during mode switching, these models primarily address component-level modeling rather than system-level operation. Moreover, the complexity and high-order nature of these dynamic models pose computational challenges for their integration into optimal operation models. In principle, low-order energy conversion models for rSOCs are preferred for efficient and reliable energy management, which can be seamlessly incorporated into optimal operation models. Furthermore, few studies consider the heat recovery potential of rSOCs in optimal operation for microgrids. While some researchers attempt to utilize waste heat during rSOC operation [9–11] attempt to reuse the released heat of rSOCs during operations, they primarily focus on waste heat at the fuel cell mode, neglecting the broader heat recovery opportunities like in the electrolysis mode with exothermic reactions. Additionally, the fitted energy conversion models used in these studies do not adequately capture the real thermal dynamics and struggle to accurately evaluate the waste heat released during different operation modes. Therefore, there remains a lack of comprehensive operation models for rSOC systems, necessitating the inclusion of physically-based energy conversion models, capturing inherent electricity–thermal–hydrogen coupling, and thermal models to assess heat recovery potential across different modes.

Aiming at addressing the existing research gaps, the generalized key novelty of this work is: unlocking the more operational flexibility of rSOCs especially leveraging their potential of waste heat recovery, through developing advanced modeling and operation solutions, facilitating enhanced economic performance of microgrids. The specific innovative contributions include:

(1) Proposing improved fundamental models for rSOC systems, accounting for their heat recovery capability and dynamic operating mode switching. These models enable the incorporation of detailed operational aspects, including electricity–heat–hydrogen coupling, mode-switching transients, and integration of recovered heat in various modes.

(2) Establishing an enhanced optimal operation model for rSOC-based microgrids, maximizing operational profits by optimizing multi-energy management. A linearized representation of the model is developed, converting it into a computationally efficient mixed-integer linear programming (MILP) formulation.

(3) Conducting a comprehensive assessment of different extents of heat recovery integration on the economic savings of rSOC-based microgrids through real-world energy island-based case studies.

The remainder of this paper is organized as follows: Section 2 presents the modeling of the rSOC system, followed by the detailed formulation of the developed operation model for the rSOC-based microgrid in Section 3. Section 4 provides descriptions of the case studies conducted and relevant analysis of the obtained results. Finally, Section 5 summarizes the main conclusions and suggests avenues for future research.

2. Modeling of rSOC system

2.1. Operation principle of rSOC system

The rSOC is technically equivalent to the combination of fuel cells and electrolyzers but are compactly implemented with a single machine, resulting in a reduced footprint and enhanced round-trip efficiency. It has the capability to operate in two modes: the fuel cell (FC) mode and the electrolysis mode (EC). In the FC mode, the rSOC system utilizes hydrogen to generate electricity, catering to the electrical demand. Conversely, in the EC mode, the system consumes electricity to produce hydrogen. The produced hydrogen can be stored for future use or supplied to the hydrogen industry and manufacturers.

Fig. 1 shows the basic schematic of an rSOC system [18]. It mainly comprises a stack for chemical reactions and a balance of plant (BOP) consisting of auxiliary units such as mass flow controller (MFC), pumps, condensers, heat exchangers (HEs), etc. Particularly, the rSOC system in this paper integrates a heat recovery unit used for recycling the waste heat inside the system. The operation of the rSOC system varies between the FC mode and the EC mode:

(1) During the FC mode, the hydrogen served as the fuel feedstock is injected into the whole system. The steam, produced by vaporizing water through the water-gas HE, is mixed with the hydrogen in the mixer to form a gas mixture. The pre-heater heats the mixed gas, which is then injected into the stack. Note that the pre-heater enables the heat exchanger to heat the mixed gas instead of using the heater [18]. Meanwhile, the atmospheric air is pumped and preheated in another

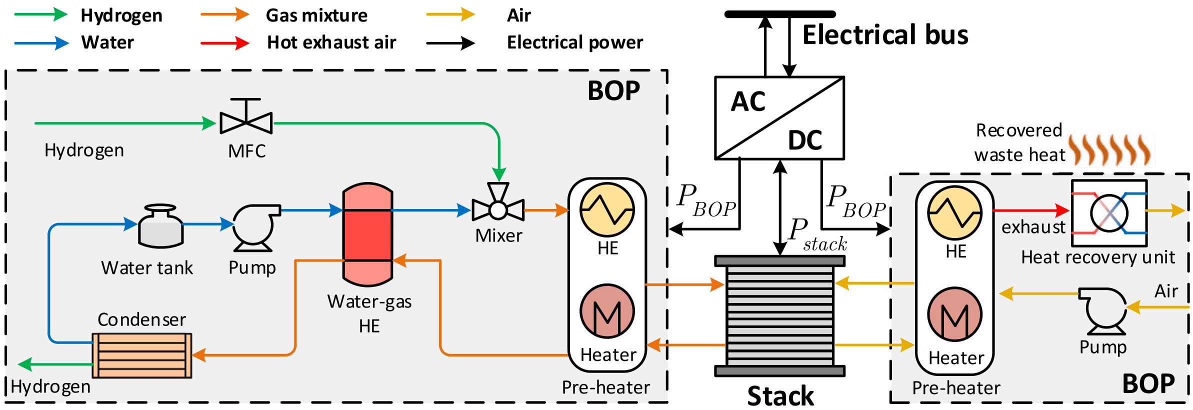

Fig. 1. Configuration of the rSOC system.

pre-heater, and then delivered to the stack to provide the necessary oxygen. The chemical reaction will produce electrical power meanwhile releasing heat which is used for heating the gas mixture and air via the HE inside the pre-heater. Besides, the heated air is exhausted from the stack into the atmosphere.

(2) During the EC mode, a significant amount of water is supplied to the stack as the primary feedstock. The mixed gas is still heated by the pre-heater. However, in this mode, the internal heater is activated instead of the heat exchanger to provide continuous heat to the stack [18]. The air is still pumped to the stack and serves as a sweep gas. The water electrolysis reaction happens in the stack to split the water into hydrogen and oxygen. Within the stack, the water electrolysis reaction takes place, separating water into hydrogen and oxygen. The hydrogen produced is condensed through the condenser and then transferred to external hydrogen tanks. Similarly, the hot exhaust air is expelled from the stack and released into the atmosphere.

It can be seen that the rSOC could release a substantial amount of waste heat at both FC mode and EC mode. Especially, the hot exhaust air emitted into the atmosphere carries significant heat energy that can be harnessed for external heat loads or district heating systems. By reusing this heat energy, the profitability of the rSOC system can be enhanced through the accumulation of heat revenue. Motivated by this potential, this paper focuses on recovering the thermal power from the hot exhaust air using a heat recovery unit. It should be emphasized that the specific methods and forms of recovering the heat energy are beyond the scope of this work, as the primary focus is on evaluating the potential profitability and value associated with the recovered heat.

2.2. Modeling of mode switching dynamics

Previous studies have shown that rSOC systems undergo a switching transient when changing between modes like FC and EC. This period represents the time needed for a complete and safe mode shift. This transient involves purging previous reactants, establishing a stable condition for the next mode within porous electrodes, as explained in [14,19]. The duration of this switching transient varies based on the system's size, ranging from 2.5 min to 30 min for different kW-class systems, according to studies [14,19,20]. Hence, when considering a relatively small time resolution (T_s) within this range, accounting for this switch transient becomes crucial for rSOC operation. To accurately capture this switching transient between FC and EC, we introduced two intermediate modes: the transition from EC to FC (TFC) and the transition from FC to EC (TEC). Furthermore, Based on the appropriate switching duration of 2.5 min to 30 min demonstrated by [14,19,20], and considering that our work utilized the same rSOC system as in [14], we maintained a 15-min time resolution, aligning with their findings. The effectiveness of 15 min to capture the switching transient has been already demonstrated by [14].

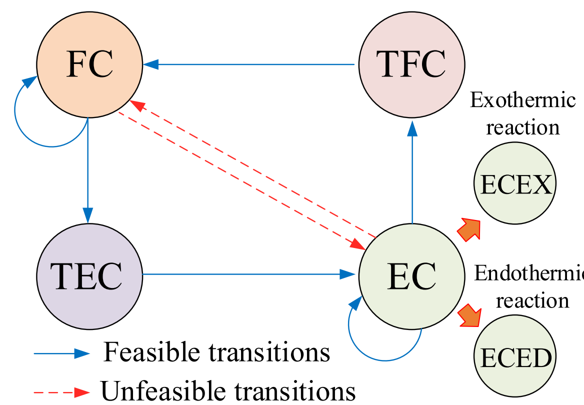

Fig. 2. Different operating modes of rSOCs and their switching dynamics.

Fig. 2 illustrates the mode-switching process in the rSOC system. In addition to the steady-state fuel cell (FC) and electrolysis (EC) modes, two transient modes of TFC and TEC are also included. In the diagram, red arrows indicate feasible transitions, while blue arrows represent unfeasible transitions, dictated by technical limitations in the rSOC system. Particularly, the direct switching between EC and FC is unfeasible, where the two switching transients must be considered.

For instance, when switching from FC to EC, the system first enters the TEC mode within a 15-min interval. During this period, the chemical reaction halts, and the operational parameters of the BOP components adjust in preparation for the EC mode. Subsequently, after an additional 15 min, the rSOC system completes the switch from TEC mode to EC mode. Therefore, a total of two time steps are necessary to complete the transition from FC to EC, following the sequence FC-to-TEC-to-EC. The same number of steps is required when transitioning from EC to FC, following the sequence EC-to-TFC-to-FC. Additionally, if the rSOC system is in FC or EC mode, it can remain unchanged in the next time step. However, if it is in TEC (or TFC) mode, it must switch to the steady-state mode EC (or FC) in the subsequent step. Additionally, the EC mode involves both exothermic and endothermic reactions, as supported by [17,20,21], each with distinct heat recovery capabilities. Differing from the perspective presented in [14], we further categorize the EC mode into two sub-modes: exothermic electrolysis mode (ECEX) and endothermic electrolysis mode (ECED). This refinement, as compared to the approach outlined in [14], allows us to effectively consider the available heat recovered within rSOC systems during both endothermic and exothermic modes.

Table 2 presents a comprehensive overview of the operating modes in the rSOC system. To determine the enabled mode, binary variables δ_i are introduced, where $\delta_i = 1$ indicates that the rSOC is operating

Table 2
Descriptions of different operation modes for rSOC.

Mode description	Mathematical representation	Heat recovery capability
FC: fuel cell mode	$\delta_{fc}=1, P_{rSOC}=-P_{fc}$	The reaction is always exothermic and recovered heat is available
ECEX: exothermic electrolysis mode	$\delta_{ecex}=1, P_{rSOC}=P_{ec}$	The reaction is exothermic and recovered heat is available
ECED: endothermic electrolysis mode	$\delta_{eced}=1, P_{rSOC}=P_{ec}$	The reaction is endothermic and requires external heat supply, thus there is no recoverable heat
TFC: transition from EC to FC	$\delta_{tfc}=1, P_{rSOC}=P_{tfc}^{N}$	No chemical reaction, no recoverable heat
TEC: transition from FC to EC	$\delta_{tec}=1, P_{rSOC}=P_{tec}^{N}$	No chemical reaction, no recoverable heat

in mode i. The mode switching constraints, as depicted in Fig. 2, can be mathematically formulated by (1)–(8). Eq. (1) ensures that only one mode can be enabled at a given time. For the electrolysis mode, the coexistence of ECEX and ECED modes is prohibited, as enforced by (2). Eqs. (3)–(6) prohibit the unfeasible mode transitions i.e. red arrows in Fig. 2. The transitions from TEC to EC and from TFC to FC at adjacent time steps are guaranteed by (7)–(8). Each mode is associated with a distinct electricity consumption (P_{rSOC}). Note that the negative sign for the power consumption in FC mode signifies the production of electricity by the rSOC system. Thus, the value of P_{rSOC} can be negative or positive, with a negative value indicating the current operation in FC mode. Furthermore, only FC mode and ECEX mode can generate recoverable waste heat, as these modes involve exothermic reactions.

$$\delta_{fc}^{(t)}+\delta_{tfc}^{(t)}+\delta_{eced}^{(t)}+\delta_{ecex}^{(t)}+\delta_{tec}^{(t)}=1 \tag{1}$$

$$\delta_{eced}^{(t)}+\delta_{ecex}^{(t)}\le 1 \tag{2}$$

$$\delta_{fc}^{(t)}+\delta_{eced}^{(t+1)}+\delta_{ecex}^{(t+1)}\le 1 \tag{3}$$

$$\delta_{fc}^{(t)}+\delta_{tfc}^{(t+1)}\le 1 \tag{4}$$

$$\delta_{eced}^{(t)}+\delta_{ecex}^{(t)}+\delta_{fc}^{(t+1)}\le 1 \tag{5}$$

$$\delta_{eced}^{(t)}+\delta_{ecex}^{(t)}+\delta_{tec}^{(t+1)}\le 1 \tag{6}$$

$$\delta_{tfc}^{(t)}-\delta_{fc}^{(t+1)}\le 0 \tag{7}$$

$$\delta_{tec}^{(t)}-\delta_{eced}^{(t+1)}-\delta_{ecex}^{(t+1)}\le 0 \tag{8}$$

2.3. Energy conversion model among electricity–heat–hydrogen

2.3.1. Conversion between electricity and hydrogen

The conversion efficiency of rSOCs between electricity and hydrogen is nonlinearly varying with its operating states such as consumed power and operating temperature. In this study, the conversion efficiency is described by an empirically derived expression from a physical-based rSOC model, as presented in [14] and formulated by (9)–(10). These equations reflect the nonlinear relationship between efficiency and electrical power as well as operating temperature, which are different in FC mode and EC mode. Notably, the ECED mode exhibits a relatively constant efficiency value (e.g., 0.74) due to its inherent physical characteristics [14]. Moreover, Eq. (10) establishes the conditions for activating the ECED and ECEX modes, which are mathematically expressed by (11) and (12). The consumption of hydrogen in the FC mode and the production of hydrogen in the EC mode are determined by (13)–(14).

$$\eta_{fc}^{(t)}=a_1\frac{T_{rSOC}^{(t)}P_{fc}^{(t)}}{n}-a_2\frac{P_{fc}^{(t)}}{n}+a_3T_{rSOC}^{(t)}-a_4\left(\frac{P_{fc}^{(t)}}{n}\right)^2 -a_5\left(T_{rSOC}^{(t)}\right)^2-a_6 \tag{9}$$

$$\eta_{ec}^{(t)}=\begin{cases}0.74, \ \textbf{if} \ \frac{P_{ec}^{(t)}}{n}\le b_1\left(T_{rSOC}^{(t)}\right)^2-b_2T_{rSOC}^{(t)}+b_3\\ b_4\frac{T_{rSOC}^{(t)}P_{ec}^{(t)}}{n}-b_5\frac{P_{ec}^{(t)}}{n}+b_6T_{rSOC}^{(t)}, \ \textbf{otherwise}\end{cases} \tag{10}$$

$$\delta_{eced}=1\Rightarrow\frac{P_{ec}^{(t)}}{n}\le b_1\left(T_{rSOC}^{(t)}\right)^2-b_2T_{rSOC}^{(t)}+b_3 \tag{11}$$

$$\delta_{ecex}=1\Rightarrow\frac{P_{ec}^{(t)}}{n}> b_1\left(T_{rSOC}^{(t)}\right)^2-b_2T_{rSOC}^{(t)}+b_3 \tag{12}$$

$$N_{fc,H_2}^{(t)}=\frac{P_{fc}^{(t)}}{\eta_{fc}^{(t)}}\frac{T_s}{LHV} \tag{13}$$

$$N_{ec,H_2}^{(t)}=P_{ec}^{(t)}\eta_{ec}^{(t)}\frac{T_s}{LHV} \tag{14}$$

2.3.2. Thermal model and heat recovery

A first-order lumped thermal model is utilized to capture the thermal dynamics of rSOCs, which describes the relationship between temperature evolution and thermal balance as expressed by (15). The thermal balance is determined by the heat generated from the chemical reaction Q_e, heat loss to the environment Q_{loss}, and heat removed through heat recovery Q_{rec}. As mentioned in Section 2.2, heat can only be produced in FC mode and ECEX mode. Therefore, a piecewise formulation is developed to calculate Q_e for different operating modes, as shown in (16). This formulation establishes the relationship among Q_e, consumed power, and conversion efficiency, enabling the coupling of electricity, heat, and hydrogen. The detailed derivation of Q_e is presented in Appendix A. The heat loss can be calculated by (17)–(18) according to [22], which is mainly influenced by the temperature difference between the rSOC's stack and the environment, thermal conductivity property and the dimension of the rSOC. The variable Q_{rec} is considered a decision variable that controls the amount of recovered heat.

$$T_{rSOC}^{(t+1)}=T_{rSOC}^{(t)}+\frac{Q_e^{(t)}-Q_{loss}^{(t)}-Q_{rec}^{(t)}}{C_{rSOC}^{lump}}T_s \tag{15}$$

$$Q_e^{(t)}=\begin{cases}0, \ \textbf{if} \ \delta_{tfc}^{(t)}\cup\delta_{tec}^{(t)}\cup\delta_{eced}^{(t)}=1\\ P_{fc}^{(t)}\left(\frac{1}{\eta_{fc}^{(t)}}-1\right), \ \textbf{if} \ \delta_{fc}^{(t)}=1\\ P_{ec}^{(t)}\left(1-\eta_{ec}^{(t)}\right), \ \textbf{if} \ \delta_{ecex}^{(t)}=1\end{cases} \tag{16}$$

$$Q_{loss}=6\left(V_{rSOC}\right)^{\frac{2}{3}}\left[\left(\frac{k_1}{3l}T_{rSOC}^3-\frac{k_2}{2l}T_{rSOC}^2-\frac{k_3}{l}T_{rSOC}\right)-\left(\frac{k_1}{3l}T_c^3-\frac{k_2}{2l}T_c^2-\frac{k_3}{l}T_c\right)\right] \tag{17}$$

$$T_c=0.0225455T_{rSOC}+279.627 \tag{18}$$

3. Problem formulation

This section focuses on the application of the developed rSOC models in the context of optimal operation for a microgrid that incorporates rSOC and other distributed energy resources (DERs). Fig. 3 illustrates the schematic of the rSOC-integrated microgrid, which aims to fulfill local electrical loads by utilizing power generated from natural gas-based combined heat and power (CHP) and DERs (such as renewable energy sources, batteries, and rSOC) as well as importing electricity from external power systems. Particularly, the microgrid possesses remarkable potential to seamlessly transition into a zero-carbon system by integrating hydrogen-based CHP plants that utilize the hydrogen produced from rSOC as their primary fuel source. This

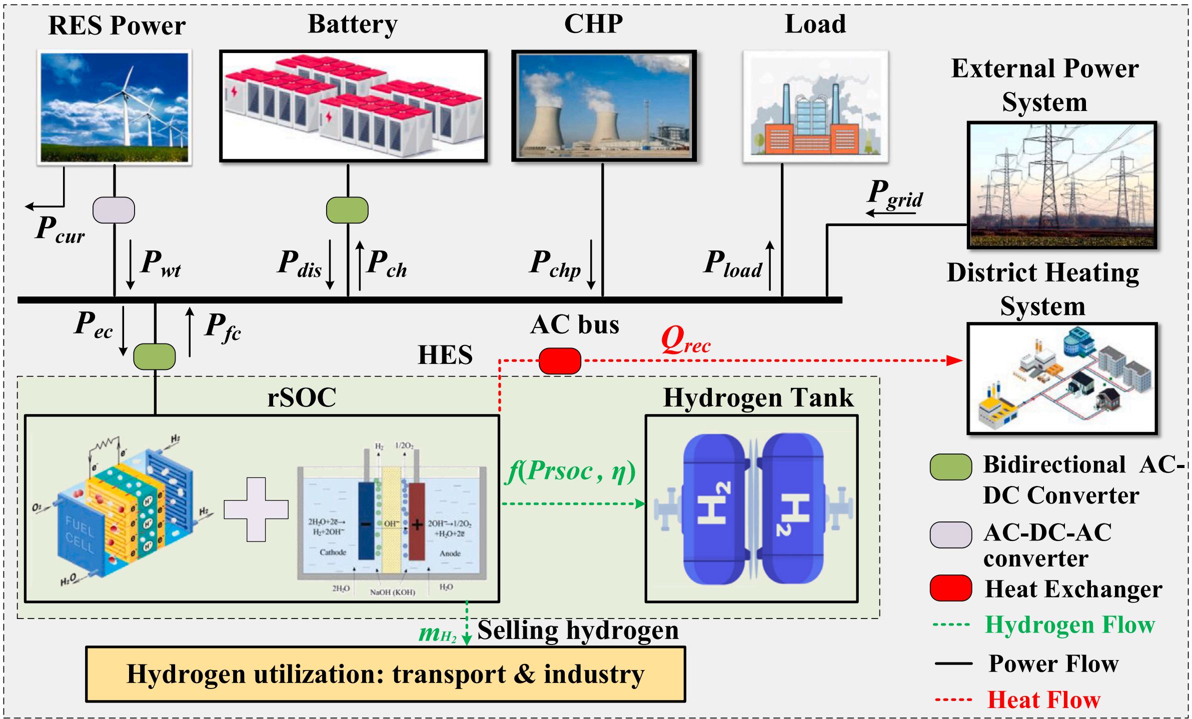

Fig. 3. Configuration of the considered rSOC-integrated microgrid.

solution allows for a significant reduction in carbon emissions and enhances energy utilization efficiency within the microgrid. Moreover, the rSOC not only produces hydrogen (m_{H_2}) but also recovers heat (Q_{rec}), offering a significant advantage for district heating systems. The recovered heat can be efficiently supplied to the district heating system, enhancing its overall energy efficiency and contributing to sustainable heating solutions. Consequently, the harmonious synergies between rSOC-based microgrids and district heating systems empower the microgrid to embrace a diverse array of energy flows, skillfully orchestrated through cross-sectoral energy transactions, thereby unlocking lucrative arbitrage opportunities. In this context, the proposed optimal operation model in this section aims to efficiently coordinate and optimize the synergy of multi-energy flows within the microgrid, specifically focusing on maximizing the overall economic benefits.

3.1. Objective function

The operation objective of the microgrid is to minimize the total operation cost considering electricity cost and revenues related to hydrogen and heat products, which can be mathematically expressed by:

$$\min \boldsymbol{J} = \sum_{t=0}^{N_p-1}\left(C_{ele}^{(t)}P_{grid}^{(t)}T_s\right) + \sum_{t=0}^{N_p-1}\left(C_{cur}^{(t)}P_{cur}^{(t)}T_s\right) - \sum_{t=0}^{N_p-1}\left(C_{heat}^{(t)}Q_{rec}^{(t)}T_s\right) - \sum_{t=0}^{N_p-1}\left(C_{H_2}^{(t)}\dot{m}_{H_2}^{(t)}T_s\right) \tag{19}$$

where $m_{H_2}^{(t)}$ is the sold hydrogen.

The first row of (19) represents the cost of electricity, which includes both the expenses incurred from purchasing power from external power systems and the penalty cost associated with curtailing RESs. The inclusion of the penalty cost encourages the maximization of RES utilization. The second row of (19) represents the revenue generated from selling hydrogen and heat produced by the rSOC system.

3.2. Constraints

The operation objective in (19) should be subjected to the technical characteristics of energy facilities in the microgrid. A few constraints need to be satisfied as follows:

(1) HES constraints

The constraints related to the hydrogen energy system (HES) consisting of the rSOC and the hydrogen tank can be characterized by (20)–(25). Eq. (20) reformulates the rSOC's temperature evolution based on the developed rSOC model (15)–(18). Particularly, an intermediate variable $\mathcal{W}$ is introduced to represent the difference between Q_e and Q_{loss}, which is expressed by (21). According to (16), $\mathcal{W}$ is expressed as a piece-wise function consisting of three components: $\mathcal{W}_1$, $\mathcal{W}_2$, $\mathcal{W}_3$ corresponding to different operation modes. $\mathcal{W}_2$ and $\mathcal{W}_3$ are bivariate nonlinear functions dependent on electrical power and operating temperature, while $\mathcal{W}_1$ is a univariate nonlinear function solely dependent on the operating temperature. To prevent excessive temperature gradients in rSOCs which adversely impact the rSOC performance, Eq. (22) constrains the temperature gradient within the threshold $\dot{T}_{max}$ (setting at 2 K/min [23]). The evolution of hydrogen level in the hydrogen tank (in per-unit) can be characterized by (23). Two intermediate variables $\mathcal{F}_1$ and $\mathcal{F}_2$ calculated using (24)–(25) are introduced to respectively represent the energy associated with the hydrogen production and consumption by the rSOC, derived from (13)–(14). Eq. (26) ensures that the relevant variables, including hydrogen level, operating temperature, sold hydrogen, and recovered heat, remain within their respective thresholds.

Besides, in order to follow the power exchange characteristics (P_{rSOC}) of the rSOC at different modes, as described in Table 2, P_{rSOC} can be formulated by (27)–(31). Additionally, the mode switching constraints described in Eqs. (1)–(8) must be taken into account.

$$T_{rSOC}^{(t+1)} = T_{rSOC}^{(t)} + \frac{\mathcal{W}^{(t)} - Q_{rec}^{(t)}}{C_{rSOC}^{lump}}T_s \quad \forall t \tag{20}$$

$$\mathcal{W}^{(t)} = Q_e^{(t)} - Q_{loss}^{(t)}$$

$$= \begin{cases} \mathcal{W}_1^{(t)}\left(T_{rSOC}^{(t)}\right), & \text{if} \quad \delta_{tfc}^{(t)} \cup \delta_{tec}^{(t)} \cup \delta_{eced}^{(t)} = 1 \\ \mathcal{W}_2^{(t)}\left(P_{fc}^{(t)}, T_{rSOC}^{(t)}\right), & \text{if} \quad \delta_{fc}^{(t)} = 1 \\ \mathcal{W}_3^{(t)}\left(P_{ec}^{(t)}, T_{rSOC}^{(t)}\right), & \text{if} \quad \delta_{ecex}^{(t)} = 1 \end{cases} \tag{21}$$

$$-\dot{T}_{max} \le \frac{T_{rSOC}^{(t+1)} - T_{rSOC}^{(t)}}{T_s} \le \dot{T}_{max} \quad \forall t \tag{22}$$

$$L_{H_2}^{(t+1)} = L_{H_2}^{(t)} + T_s \frac{\mathcal{F}_2^{(t)} - \mathcal{F}_1^{(t)} - \dot{m}_{H_2} LHV}{E_{H_2}} \quad \forall t \tag{23}$$

$$\mathcal{F}_1^{(t)} = \frac{P_{fc}^{(t)}}{\eta_{fc}^{(t)}} \quad \forall t \tag{24}$$

$$\mathcal{F}_2^{(t)} = \eta_{ec}^{(t)} P_{ec}^{(t)} \quad \forall t \tag{25}$$

$$\alpha^{min} \le \alpha^{(t)} \le \alpha^{max} \Big|_{\alpha = L_{H_2}, T_{rSOC}, \dot{m}_{H_2}, Q_{rec}} \quad \forall t \tag{26}$$

$$P_{rSOC}^{(t)} = P_{ec}^{(t)} - P_{fc}^{(t)} + P_{tec}^{(t)} + P_{tfc}^{(t)} \quad \forall t \tag{27}$$

$$\delta_{ec}^{(t)} P_{ec}^{min} \le P_{ec}^{(t)} \le \delta_{ec}^{(t)} P_{ec}^{max} \quad \forall t \tag{28}$$

$$\delta_{fc}^{(t)} P_{fc}^{min} \le P_{fc}^{(t)} \le \delta_{fc}^{(t)} P_{fc}^{max} \quad \forall t \tag{29}$$

$$\delta_{tec}^{(t)} P_{tec}^{N} \le P_{tec}^{(t)} \le \delta_{tec}^{(t)} P_{tec}^{N} \quad \forall t \tag{30}$$

$$\delta_{tfc}^{(t)} P_{tfc}^{N} \le P_{tfc}^{(t)} \le \delta_{tfc}^{(t)} P_{tfc}^{N} \quad \forall t \tag{31}$$

(2) Battery constraints

The capacity level of the battery (in per unit), influenced by its charging and discharging power, is described by (32). To ensure the capacity level and the charging/discharging power of the battery remain within their limits, constraints are imposed as shown in (33)–(34). Eq. (35) guarantees that the battery cannot simultaneously operate in both charging and discharging modes.

$$L_b^{(t+1)} = L_b^{(t)} + \frac{\left(P_{ch}^{(t)} - P_{dis}^{(t)}\right) T_s}{E_b} \quad \forall t \tag{32}$$

$$L_b^{min} \le L_b^{(t)} \le L_b^{max} \quad \forall t \tag{33}$$

$$\delta_\beta^{(t)} P_\beta^{min} \le P_\beta^{(t)} \le \delta_\beta^{(t)} P_\beta^{max} \Big|_{\beta = dis, ch} \quad \forall t \tag{34}$$

$$\delta_{dis}^{(t)} + \delta_{ch}^{(t)} \le 1 \quad \forall t \tag{35}$$

(3) Power balance constraint

The power balance in the microgrid must be satisfied for its stable operation, which can be formulated by (36). Eq. (37) establishes the limits for the purchased power from external power systems and the curtailed RES power. Furthermore, constraint (38) ensures that the microgrid avoids the inefficient and non-economic operation of simultaneously purchasing power from external grids and curtailing RES power.

$$P_{res}^{(t)} + P_{chp}^{(t)} + P_{dis}^{(t)} + P_{grid}^{(t)} = P_{ch}^{(t)} + P_{rSOC}^{(t)} + P_{cur}^{(t)} + P_{load}^{(t)} \quad \forall t \tag{36}$$

$$\delta_\gamma^{(t)} P_\gamma^{min} \le P_\gamma^{(t)} \le \delta_\gamma^{(t)} P_\gamma^{max} \Big|_{\gamma = grid, cur} \quad \forall t \tag{37}$$

$$\delta_{grid}^{(t)} + \delta_{cur}^{(t)} \le 1 \quad \forall t \tag{38}$$

3.3. Linearization process of the operation model

The operation model is obtained with the objective function of (19) which is subjected to constraints (1)–(12) and (20)–(38). However, this model is challenging to solve due to several implicit and nonlinear constraints, including: (1) the implicit and nonlinear constraint (21) involving conditional expressions and nonlinear functions ($\mathcal{W}_1, \mathcal{W}_2, \mathcal{W}_3$); (2) constraints (24)–(25), which are nonlinear functions according to (9)–(10); (3) the nonlinear expressions (11)–(12) and the implicit relationship with δ_{eced} and δ_{ecex}. To facilitate efficient solution, these constraints need to be equivalently transformed into linearized forms. Therefore, this subsection will provide a detailed linearization process to reformulate the operation model as an MILP model, which can be effectively solved using commercial solvers like Gurobi [24].

(1) Explicit transformation for conditional constraints in (11)–(12) and (21)

Based on the big-M method, the conditional form of (11)–(12) can be reformulated as equivalent linear constraints (39)–(40). This equivalence can be demonstrated as follows: if $\delta_{eced}^{(t)} = 1$, Eq. (39) imposes the exact same constraint as (11); whereas if $\delta_{eced}^{(t)} = 0$, Eq. (39) becomes a non-binding constraint due to the large value of M. Hence, constraint (39) has the same effect on the operation model as constraint (11). By following a similar analysis procedure, the equivalence between (12) and (40) can also be established. Notably, a small value σ is introduced to convert the strong inequality into a weak inequality for easier solving. Likewise, the big-M method can be applied to transform (21) into a set of linear constraints, specifically (41)–(44). Considering the constraint imposed by (1) among these binary variables, the equivalence of this transformation can be proved based on the same analysis procedure.

$$\frac{P_{ec}^{(t)}}{n} - \left(b_1 \left(T_{rSOC}^{(t)}\right)^2 - b_2 T_{rSOC}^{(t)} + b_3\right) \le (1 - \delta_{eced}^{(t)}) M \tag{39}$$

$$\frac{P_{ec}^{(t)}}{n} - \left(b_1 \left(T_{rSOC}^{(t)}\right)^2 - b_2 T_{rSOC}^{(t)} + b_3\right) \ge (\delta_{ecex}^{(t)} - 1) M + \sigma \tag{40}$$

$$\left(\delta_{eced}^{(t)} + \delta_{tec}^{(t)} + \delta_{tfc}^{(t)} - 1\right) M + \mathcal{W}_1^{(t)} \le \mathcal{W}^{(t)} \tag{41}$$

$$\mathcal{W}^{(t)} \le \left(1 - \delta_{eced}^{(t)} - \delta_{tec}^{(t)} - \delta_{tfc}^{(t)}\right) M + \mathcal{W}_1^{(t)} \tag{42}$$

$$\left(\delta_{fc}^{(t)} - 1\right) M + \mathcal{W}_2^{(t)} \le \mathcal{W}^{(t)} \le \left(1 - \delta_{fc}^{(t)}\right) M + \mathcal{W}_2^{(t)} \tag{43}$$

$$\left(\delta_{ecex}^{(t)} - 1\right) M + \mathcal{W}_3^{(t)} \le \mathcal{W}^{(t)} \le \left(1 - \delta_{ecex}^{(t)}\right) M + \mathcal{W}_3^{(t)} \tag{44}$$

(2) Linearization for nonlinear expressions in (11)–(12) and (24)–(25)

Note that although the constraints (39)–(40) have been explicitly formulated, they still contain nonlinearity due to the presence of the nonlinear expression (45), which originates from (11)–(12). To address this, we introduce an intermediate variable $\mathcal{H}$ to represent the nonlinear expression, which is a function of the operating temperature. Thus, Eqs. (39)–(40) can be rewritten as (46)–(47).

$$\mathcal{H} = b_1 \left(T_{rSOC}^{(t)}\right)^2 - b_2 T_{rSOC}^{(t)} + b_3 \tag{45}$$

$$\frac{P_{ec}^{(t)}}{n} - \mathcal{H} \le (1 - \delta_{eced}^{(t)}) M \tag{46}$$

$$\frac{P_{ec}^{(t)}}{n} - \mathcal{H} \ge (\delta_{ecex}^{(t)} - 1) M + \sigma \tag{47}$$

It can be seen that there are six nonlinear functions including univariate functions $\mathcal{W}_1$, $\mathcal{H}$, as well as bivariate functions $\mathcal{W}_2$, $\mathcal{W}_3$, $\mathcal{F}_1$, $\mathcal{F}_2$. In this paper, the methodology of piecewise linearization is adopted to linearize these nonlinear functions. For the linearization of the univariate functions, the well-established approach based on the Special Ordered Set of Type 2 (SOS2) introduced by [25] is utilized. The SOS2-based approach approximates the original function value $f(x)$ at point x by satisfying a set of linear constraints, as shown in (48)–(52). To handle the linearization of bivariate functions, we employ an improved version of SOS2 known as SOS3, proposed by [26]. The SOS3-based approach utilizes linear constraints, as presented in (53)–(59), to obtain an approximate value $\tilde{f}$ for a bivariate function $f(x, y)$. By employing the SOS2 and SOS3 based approaches, the six nonlinear functions in the operation model can be effectively linearized. The detailed implementation procedure is provided in Algorithms 1 and 2 (as presented in Tables 3–4). These two algorithms replace the original intermediate variables associated with the six nonlinear functions with new variables bound by a set of linear constraints, as depicted in (60)–(61). It is worth noting that the superscript t is not explicitly shown

Table 3
Piece-wise linearization for $\mathcal{W}_1$, $\mathcal{H}$.

Algorithm 1: SOS2 based linearization algorithm

Input: a number of sampling points $T_{rSOC,i}$ **for** $i \in [1, n]$
Ouput: A set of linear constraints for calculating approximate value of $\mathcal{W}_1$,$\mathcal{H}$
Calculating the function value $\mathcal{W}_{1,i}$, $\mathcal{H}_i$ at the point $T_{rSOC,i}$ based on (20)–(21) and (45)
Let: $x = T_{rSOC}$, $f = \{\mathcal{W}_1, \mathcal{H}\}$
Estimate the approximate value $\tilde{f}$ according to (48)–(52).
$\mathcal{W}_1 = \tilde{\mathcal{W}}_1$, when $f = \mathcal{W}_1$
$\mathcal{H} = \tilde{\mathcal{H}}$, when $f = \mathcal{H}$
return $\mathcal{W}_1 = \tilde{\mathcal{W}}_1$, $\mathcal{H} = \tilde{\mathcal{H}}$ and their corresponding SOS2 constraints i.e. (48)–(52)

in these intermediate variables for simplicity of expression and ease of understanding, but they are indeed temporal variables.

$$\sum_{i=1}^{n-1} l_i = 1, \quad l_0 = 0, \quad l_n = 0 \tag{48}$$

$$\omega_i \leq l_{i-1} + l_i \quad i \in [1, n] \tag{49}$$

$$\sum_{i=1}^{n} \omega_i = 1 \tag{50}$$

$$x = \sum_{i=1}^{n} \omega_i x_i \tag{51}$$

$$\tilde{f} = \sum_{i=1}^{n} \omega_i f(x_i) \tag{52}$$

where $l_i \in \mathbb{B}$ is a binary variable; $\omega_i \in \mathbb{R}$ is a continuous variable; x_i and $f(x_i)$ denote the input sampling points and corresponding function values; n is the number of sampling points for the variable x.

$$\sum_{i=1}^{n-1} \sum_{j=1}^{m-1} \left(h_{ij}^u + h_{ij}^l \right) = 1 \tag{53}$$

$$\lambda_{ij} \leq h_{ij}^u + h_{ij}^j + h_{i,j-1}^u + h_{i-1,j-1}^l + h_{i-1,j-1}^u + h_{i-1,j}^l \quad \forall i \in [1, n], j \in [1, m] \tag{54}$$

$$h_{0j}^* = h_{nj}^* = h_{i0}^* = h_{im}^* = 0 \,|_{*=u,l} \quad \forall i \in [1, n], j \in [1, m] \tag{55}$$

$$\sum_{i=1}^{n} \sum_{j=1}^{m} \lambda_{ij} = 1 \tag{56}$$

$$x = \sum_{i=1}^{n} \sum_{j=1}^{m} \lambda_{ij} x_i \tag{57}$$

$$y = \sum_{i=1}^{n} \sum_{j=1}^{m} \lambda_{ij} y_j \tag{58}$$

$$\tilde{f} = \sum_{i=1}^{n} \sum_{j=1}^{m} \lambda_{ij} f\left(x_i, y_j\right) \tag{59}$$

where $h_{ij}^u, h_{ij}^l \in \mathbb{B}$ is a binary variable; $\lambda_{ij} \in \mathbb{R}$ is a continuous variable; (x_i, y_j) is the input sampling points while $f(x_i, y_j)$ is the corresponding function value; n, m are the number of sampling points for the variable x, y,respectively.

$$\forall\, G_1 = \left\{ \mathcal{W}_1, \mathcal{H} \right\}: \quad G_1 = \tilde{G_1}, \quad (48)\text{–}(52) \tag{60}$$

$$\forall\, G_2 = \left\{ \mathcal{W}_2, \mathcal{W}_3, \mathcal{F}_1, \mathcal{F}_2 \right\}: \quad G_2 = \tilde{G_2}, \quad (53)\text{–}(59) \tag{61}$$

3.4. Summary of the operation model

Based on the linearization process, the operation model can be converted into an MILP model which can be mathematically described as (62). This MILP model can be effectively and efficiently solved by employing well-established commercial solvers such as Gurobi.

Table 4
Piece-wise linearization for $\mathcal{W}_2$, $\mathcal{W}_3$, $\mathcal{F}_1$, $\mathcal{F}_2$.

Algorithm 2: SOS3 based linearization algorithm

Input: a number of sampling points $X_{1,ij} = \left(P_{fc,i}, T_{rSOC,j}\right)$, $X_{2,ij} = \left(P_{ec,i}, T_{rSOC,j}\right)$ **for** $i \in [1, n], j \in [1, m]$
Ouput: A set of linear constraints for calculating approximate value of $\mathcal{W}_2$,$\mathcal{W}_3$,$\mathcal{F}_1$,$\mathcal{F}_2$
1 Calculating the function value $\mathcal{W}_{2,ij}$,$\mathcal{F}_{1,ij}$ at the point $X_{1,ij}$ based on (16)–(18), (21)
2 Calculating the function value $\mathcal{W}_{3,ij}$,$\mathcal{F}_{2,ij}$ at the point $X_{2,ij}$ based on (9)–(10) and (24)–(25)
3 **Let:** $x = X_1$, $f = \{\mathcal{W}_2, \mathcal{F}_1\}$
4 Estimate the approximate value $\tilde{f}$ according to (53)–(59).
5 **Let:** $x = X_2$, $f = \{\mathcal{W}_3, \mathcal{F}_2\}$ and repeat step 3
6 $\mathcal{W}_2 = \tilde{\mathcal{W}}_2$, when $f = \mathcal{W}_2$
7 $\mathcal{W}_3 = \tilde{\mathcal{W}}_3$, when $f = \mathcal{W}_3$
8 $\mathcal{F}_1 = \tilde{\mathcal{F}}_1$, when $f = \mathcal{F}_1$
9 $\mathcal{F}_2 = \tilde{\mathcal{F}}_2$, when $f = \mathcal{F}_2$
10 **return** $\mathcal{W}_2 = \tilde{\mathcal{W}}_2$, $\mathcal{W}_3 = \tilde{\mathcal{W}}_3$, $\mathcal{F}_1 = \tilde{\mathcal{F}}_1$, $\mathcal{F}_2 = \tilde{\mathcal{F}}_2$, and their corresponding SOS3 constraints i.e. (53)–(59)

$$\begin{aligned}
&\min_{\mathbf{U},\mathbf{B}} \quad (19) \\
&\text{s.t.} \quad (1)\text{–}(9), (20), (22)\text{–}(23), (26)\text{–}(38), (41)\text{–}(44), \\
&\qquad (46)\text{–}(47), (60)\text{–}(61) \\
&\mathbf{U} = \Big\{ P_{grid}^{(t)}, P_{cur}^{(t)}, P_{dis}^{(t)}, P_{ch}^{(t)}, P_{rSOC}^{(t)}, P_{fc}^{(t)}, P_{ec}^{(t)}, P_{tec}^{(t)}, P_{tfc}^{(t)}, Q_{rec}^{(t)}, \dot{m}_{\mathrm{H}_2}^{(t)}, \\
&\qquad L_{\mathrm{H}_2}^{(t)}, L_b^{(t)}, T_{rSOC}^{(t)}, \tilde{\mathcal{W}}^{(t)}, \tilde{\mathcal{W}}_1^{(t)}, \tilde{\mathcal{W}}_2^{(t)}, \tilde{\mathcal{W}}_3^{(t)}, \tilde{\mathcal{F}}_1^{(t)}, \tilde{\mathcal{F}}_2^{(t)}, \tilde{\mathcal{H}}^{(t)}, \omega_i^{(t)}, \lambda_{ij}^{(t)} \Big\} \\
&\mathbf{B} = \Big\{ \delta_{grid}^{(t)}, \delta_{cur}^{(t)}, \delta_{dis}^{(t)}, \delta_{ch}^{(t)}, \delta_{fc}^{(t)}, \delta_{tfc}^{(t)}, \delta_{ecex}^{(t)}, \delta_{eced}^{(t)}, \delta_{tec}^{(t)}, l_i^{(t)}, h_{ij}^{u,(t)}, h_{ij}^{l,(t)} \Big\}
\end{aligned} \tag{62}$$

where $\mathbf{U}$ and $\mathbf{B}$ are respectively the set of continuous and binary variables.

4. Case studies

4.1. Case descriptions

To validate the proposed operation method, comparative case studies are conducted based on the microgrid (see Fig. 3) that emulates the system setup and energy portfolios of the Danish Bornholm energy island. Historical operation data of the island in 2018 are utilized as input parameters to the proposed operation model, including renewable power production, power production of CHP plants, and electrical demands. The spot electricity price in the Danish electricity market was employed to calculate the electricity cost. These input data are shown in Appendix B. The parameters of the rSOC system are oriented from [14]. In most of the presented results, the hydrogen price was set at 1 €/kg based on a long-term price prediction [27,28], and the heat price was set at 52 €/MWh. However, a sensitivity analysis was performed to evaluate the impact of the heat price on the benefits derived from rSOC's heat recovery. Different heat price levels were considered in the analysis. The time resolution of the operation model is 15 min in which the transition between rSOC's operation modes must be thus considered. Furthermore, two other benchmark operation models were simulated for comparison with the proposed model. The three models are described as follows:

(a) Model A: the proposed model
(b) Model B: the operating temperature of the rSOC is fixed at 1023 K (following the assumption made in [9–12])
(c) Model C: no heat recovery [14]

Additionally, the impact of linearization approximation on the performance of the proposed model is also evaluated by considering different linearization accuracy levels.

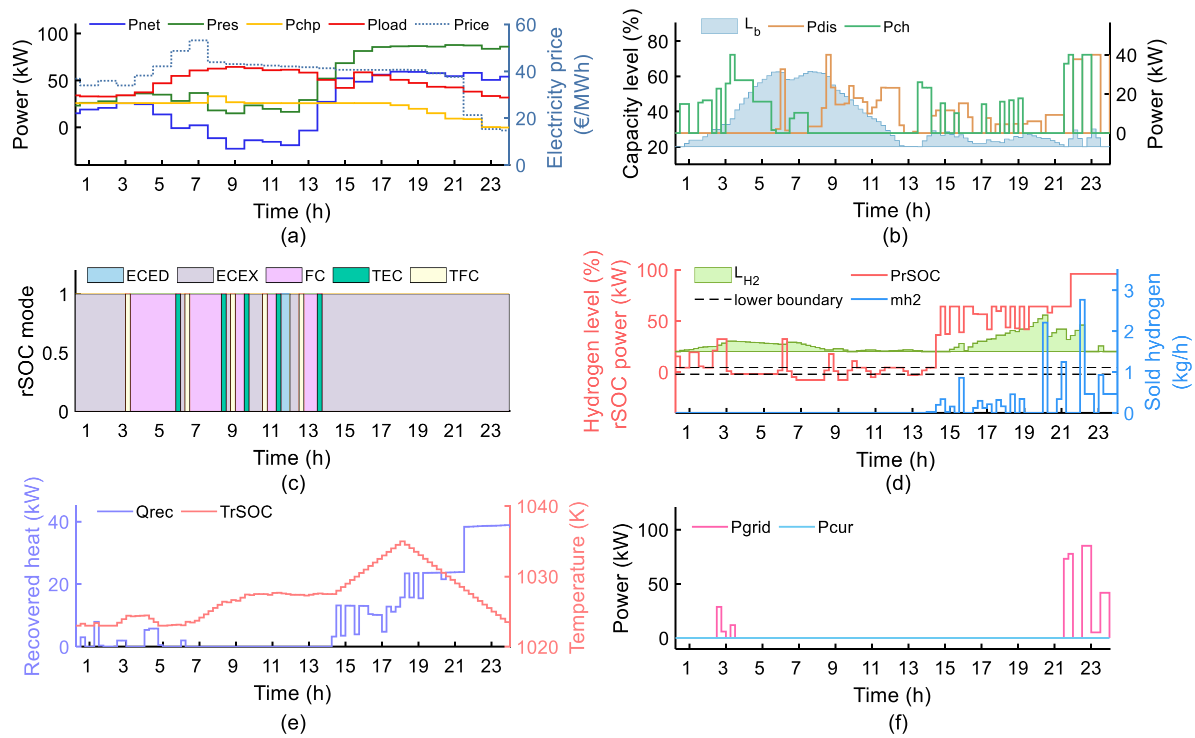

Fig. 4. One-day operation results of the microgrid: (a) input energy and price profiles; (b) operation details of battery; (c) operating mode of rSOC; (d) operation details of rSOC power, hydrogen production and consumption; (e) operating temperature and recovered heat of rSOC; (f) purchased power and curtailed wind power.

4.2. Performance evaluation of the proposed model

4.2.1. Operation results

Fig. 4 illustrates the one-day operation results of the microgrid using the proposed operation model. Overall, the model effectively schedules the battery and rSOC based on the network power levels and electricity prices. An example of this is observed during the period of 21:00–24:00, where there is a surplus of network power and relatively low electricity prices, as shown in Fig. 4(a). In response to this, the surplus power is utilized by charging the battery and operating the rSOC in the electrolyzer mode to produce hydrogen, as seen from Fig. 4(b) and (d). Furthermore, during this period, the microgrid purchases a significant amount of electricity, as shown in Fig. 4(f). This is because the electricity cost is lower than the revenue generated from selling hydrogen and heat produced using the purchased electricity. As a result, additional profits can be obtained through this operation strategy.

In addition, Fig. 4(c) indicates that the proposed model can achieves mode switching for the rSOC. Particularly, the rSOC's power at both FC mode and EC mode is effectively controlled beyond their lower thresholds (see Fig. 4(d)). Note that the negative rSOC's power corresponds to the FC mode while the positive power represents the power consumption at the EC mode. Moreover, Fig. 4(e) shows that the proposed model can enable to recover the waste heat from the rSOC. More recovered heat can be obtained by decreasing the operating temperature, which is essentially due to releasing the stored heat in the rSOC.

4.2.2. Comparisons between the proposed model with other models

Fig. 5 compares economic performance between the proposed model (Model A) and the other two benchmark models (Model B and Model C). Overall, all three operation models can achieve economic savings for the microgrid through optimal energy management, driven by economic incentives. However, the difference between Model A and Model C indicates that integrating the heat recovery strategy in the operation model contributes to higher profits, with an average daily increase of approximately 18 € during a one-week operation. This

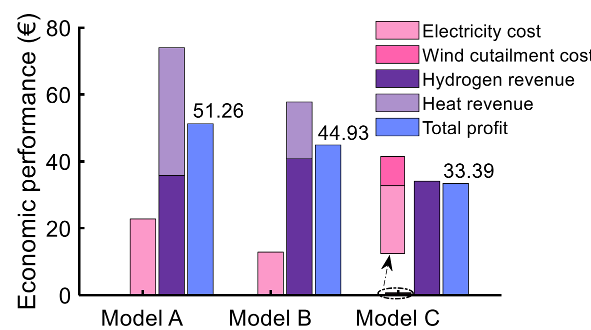

Fig. 5. Comparisons of average daily economic performance among three operation models in a one-week operation.

increase is primarily attributed to the additional revenue generated by selling the recovered waste heat from the rSOC, while also eliminating wind curtailment costs. Additionally, comparing Model A to Model B reveals that the flexibility derived from the operating temperature adjustment of rSOC can be helpful in increasing the economic savings for the microgrid. Thus, enabling the controllability of rSOC's temperature within the security threshold is recommended to release more operational flexibility for supporting system operations.

Although Model A brings a better economic performance compared to Model C, it introduces more complexity to the optimization model, posing challenges in computational efficiency. As shown in Fig. 6, Model A requires more time to compute the operation model compared to Model C. This is mainly due to the introduction of numerous auxiliary variables for linearizing the nonlinear constraints related to thermal dynamics in Model A. In contrast, Model C does not involve these nonlinear constraints as it does not consider heat recovery, making it faster to solve. Furthermore, as the scheduling horizon increases, the computational time of Model A rapidly increases.

Furthermore, the effectiveness of the proposed method under different time resolutions is examined. The operational model can be

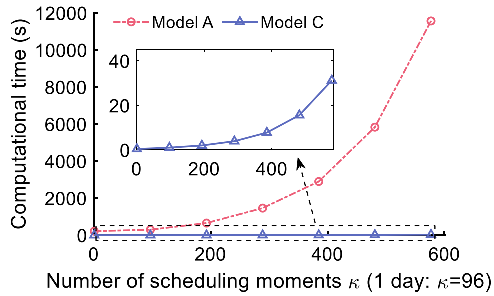

Fig. 6. Comparisons of computational performance between Model A and Model C.

Table 5
Comparisons of average daily profits (€) among three operation models for the microgrid under different time resolutions.

Time resolution (min)	Model A	Model B	Model C
$T_s = 15$	51.26	44.93	33.39
$T_s = 10$	10.64	3.16	9.04
$T_s = 5$	21.17	11	8.65
$T_s = 2$	46.32	41.13	15.71

fine-tuned using the model parameter T_s, effortlessly allowing for conducting the optimal operation of rSOC systems in scenarios with different time resolutions. By setting different T_s, we conduct a comparative analysis of daily total profits obtained using different operation models with varying time resolutions, as illustrated in Table 5. The results clearly indicate that our proposed operation model (Model A) consistently achieves maximum profits across different time resolutions. This robust performance underscores the effectiveness of our model, even when applied to rSOC systems with shorter mode-switching times.

It is concluded that the proposed model (Model A) effectively captures the operational details of rSOC systems, including operation mode switching and enabling heat recovery capabilities. By considering these details, the model provides a more reliable schedule for rSOC systems. Additionally, the model achieves cost-effective energy management for microgrids through electricity–heat–hydrogen energy transactions. However, it is important to note that the proposed model has a relatively higher computational burden. Therefore, it is more beneficial for conducting short-term optimal operations, such as daily operations, with minute-level or lower resolutions. For longer-term planning or large-scale systems, where computational efficiency is critical, alternative approaches may need to be considered, such as choosing simpler model (like Model A) by simplifying operational details, or utilizing higher-efficient solving algorithms. In addition, it is demonstrated that the proposed operation model exhibits good robustness and adaptability in implementing the optimal operation of rSOCs with different mode-switching times.

4.3. Impact of heat price

Fig. 5 has demonstrated the profitability of rSOC's heat recovery at a specific heat price (i.e. 52 €/MWh). In order to clarify the impact of the heat price on profitability, a sensitivity analysis of profitability is further conducted. As depicted in Fig. 7, it reveals that the profitability of Model A and Model B is getting better as the heat price increases because higher revenue via selling the recovered heat will be earned. This will not happen in Model C because it is disabled to obtain revenue from heat transactions. Moreover, the additional profit generated by Model A compared to the other two models increases as the heat price rises. This indicates that the operational flexibility provided by rSOC systems, through enabling heat recovery and temperature adjustment, becomes more valuable and profitable in scenarios where the cost of heat supply is quite high.

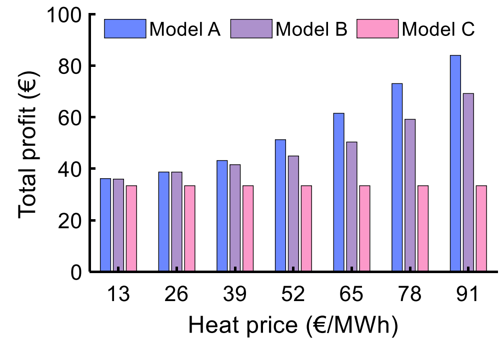

Fig. 7. Economic performance of different models at different heat prices.

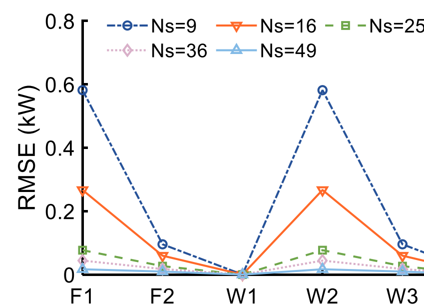

Fig. 8. RMSE for the six nonlinear expressions under different N_s.

Table 6
Computational time of the proposed operation model under different N_s.

Number of sampling points for linearization N_s	Computational time (s)
$N_s = 9$	127.36
$N_s = 16$	180.91
$N_s = 25$	267.80
$N_s = 36$	303.00
$N_s = 49$	349.50

4.4. Evaluation of linearization approximation

The impact of linearization approximation on the proposed model is also analyzed. Fig. 8 shows the root-mean-square error (RMSE) calculated for the six nonlinear expressions in the proposed model, based on their linearized values compared to the actual values. It is observed that increasing the number of sampling points (N_s) for linearization leads to a smaller RMSE, indicating a closer approximation to the actual nonlinear values. Nevertheless, Table 6 also indicates that the higher N_s results in increased computational time. Hence, there is a conflict between model accuracy and computational burden. It is therefore recommended to determine a reasonable linearization approximation level based on the specific scenario and the desired performance preference. For example, if fast and rough evaluations are required, a smaller N_s may be preferable to minimize computational time. On the other hand, if accurate evaluations are essential, even at the expense of longer computational time, a larger N_s can be chosen.

5. Conclusion

This work investigates the benefits of optimal energy management from rSOCs for maximizing the economic performance of rSOC-based microgrids, from the perspectives of modeling and operating. Fundamental models of rSOCs are developed to effectively incorporate more operational details into the operation models of microgrids, including electricity–heat–hydrogen interactions, mode switching process, and heat recovery potentials. The results reveal that:

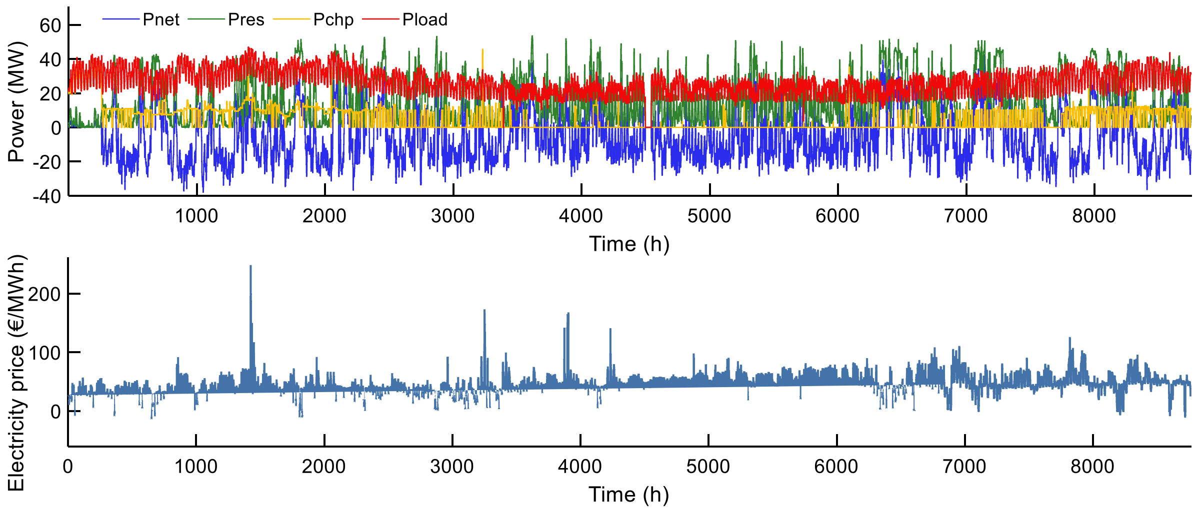

Fig. 9. Input data for the proposed operation model.

(1) The proposed operation model can reasonably schedule the battery and rSOC in response to variations in exchanged power between the microgrid and external power grids, and electricity prices. In particular, the model can enable rSOC to operate at different operation modes meanwhile drive the heat recovery of the rSOC.

(2) The integration of the heat recovery strategy in the operation model significantly improves the economic benefits of microgrids, particularly in scenarios with high heating costs. Additionally, allowing a wider temperature range for the rSOC further enhances economic performance through the proposed optimal operation method.

(3) Due to incorporating more operational details, the proposed operation model is a bit time-consuming to solve. Achieving a balanced compromise between the model's linearization accuracy and computational burden necessitates careful consideration of appropriate linearization approximation levels.

Regarding future work, a crucial aspect will entail integrating a comprehensive network model of the district heating system to encompass comprehensive and practical constraints pertaining to the heat recovery aspects of rSOCs. Furthermore, it is imperative to examine the feasibility of replacing CHPs with rSOCs for heat supply to district heating systems, and to further explore efficient solutions for achieving zero-carbon heat supply through rSOCs for district heating systems. Additionally, another valuable extension would be to integrate grid ancillary services into the proposed operation model. This integration would enable the microgrid to coordinate rSOCs and other DERs to actively participate in offering grid services in electricity markets, thereby amplifying the economic benefits of rSOC-based microgrids.

CRediT authorship contribution statement

Chunjun Huang: Writing – original draft, Visualization, Validation, Methodology, Investigation, Formal analysis, Conceptualization. **Goran Strbac:** Writing – review & editing, Supervision, Resources, Funding acquisition. **Yi Zong:** Writing – review & editing, Supervision, Methodology, Data curation. **Shi You:** Writing – review & editing, Supervision, Resources, Formal analysis. **Chresten Træholt:** Writing – review & editing, Visualization, Supervision. **Nigel Brandon:** Writing – review & editing, Resources, Data curation. **Jiawei Wang:** Writing – review & editing, Visualization. **Hossein Ameli:** Resources, Data curation.

Declaration of competing interest

The authors declare that they have no known competing financial interests or personal relationships that could have appeared to influence the work reported in this paper.

Data availability

Data will be made available on request.

Acknowledgments

This work is supported by the EPSRC, United Kingdom-funded research project "High efficiency reversible solid oxide cells for the integration of offshore renewable energy using hydrogen" under grant number EP/W003597/1. In addition, The Ph.D. student, Chunjun Huang, is jointly supported by the China Scholarship Council and Technical University of Denmark.

Appendix A

According to [21], whether an rSOC system produces thermal power or requires external thermal power depends on the operation mode and the difference between the cell voltage (U_{cell}) and the thermo-neutral voltage (U_{th}). In the FC mode, the reaction is always exothermic where U_{cell} is larger than U_{th}, thus always producing thermal power ($Q_e > 0$). However, only in the electrolysis mode with the exothermic reaction (i.e. ECEX mode in which the U_{cell} is larger than U_{th}) [21], the rSOC systems can generate heat otherwise external heat should be supplied. Therefore, produced thermal power of rSOC systems during chemical reactions can be expressed by:

$$Q_e = \begin{cases} \left(U_{tn} - U_{cell}\right) nI_{rSOC}, & \textbf{if} \quad \delta_{fc} = 1 \\ \left(U_{cell} - U_{tn}\right) nI_{rSOC}, & \textbf{if} \quad \delta_{ecex} = 1 \end{cases} \tag{A.1}$$

From the perspective of energy conversion, the system efficiency of rSOC can be also formulated by [14,21]:

$$\eta_{fc} = \frac{U_{cell}}{U_{tn}\eta_F} \tag{A.2}$$

$$\eta_{ec} = \frac{U_{tn}\eta_F}{U_{cell}} \tag{A.3}$$

where η_F is the Faraday efficiency which is closed to 100% [5].

By substituting (A.2)–(A.3) into (A.4), the produced thermal power can be reformulated as:

$$Q_e = \begin{cases} P_{fc}\left(\dfrac{1}{\eta_{fc}} - 1\right), & \textbf{if} \quad \delta_{fc} = 1 \\ P_{ec}\left(1 - \eta_{ec}\right), & \textbf{if} \quad \delta_{ecex} = 1 \end{cases} \tag{A.4}$$

Appendix B

The input data for the operation model is shown in Fig. 9, including the historical data of power production and consumption for Danish Bornholm island in 2018 and electricity price in 2018.

References

[1] European Commission. European Green Deal: EU agrees stronger legislation to accelerate the rollout of renewable energy. 2023, URL https://ec.europa.eu/commission/presscorner/detail/en/IP_23_2061.
[2] Gielen D, Boshell F, Saygin D, Bazilian MD, Wagner N, Gorini R. The role of renewable energy in the global energy transformation. Energy Strategy Rev 2019;24(June 2018):38–50. http://dx.doi.org/10.1016/j.esr.2019.01.006.
[3] Energy storage for electricity generation and related processes: Technologies appraisal and grid scale applications. Renew Sustain Energy Rev 2018;94(June):804–21. http://dx.doi.org/10.1016/j.rser.2018.06.044.
[4] Arsad AZ, Hannan MA, Al-Shetwi AQ, Mansur M, Muttaqi KM, Dong ZY, Blaabjerg F. Hydrogen energy storage integrated hybrid renewable energy systems: A review analysis for future research directions. Int J Hydrogen Energy 2022;47(39):17285–312. http://dx.doi.org/10.1016/j.ijhydene.2022.03.208.
[5] Buttler A, Spliethoff H. Current status of water electrolysis for energy storage, grid balancing and sector coupling via power-to-gas and power-to-liquids: A review. Renew Sustain Energy Rev 2018;82(February 2017):2440–54. http://dx.doi.org/10.1016/j.rser.2017.09.003.
[6] Yue M, Lambert H, Pahon E, Roche R, Jemei S, Hissel D. Hydrogen energy systems: A critical review of technologies, applications, trends and challenges. Renew Sustain Energy Rev 2021;146(April):111180. http://dx.doi.org/10.1016/j.rser.2021.111180.
[7] Parra D, Valverde L, Pino FJ, Patel MK. A review on the role, cost and value of hydrogen energy systems for deep decarbonisation. Renew Sustain Energy Rev 2019;101(July 2018):279–94. http://dx.doi.org/10.1016/j.rser.2018.11.010.
[8] Jensen SH, Graves C, Mogensen M, Wendel C, Braun R, Hughes G, Gao Z, Barnett SA. Large-scale electricity storage utilizing reversible solid oxide cells combined with underground storage of CO2 and CH4. Energy Environ Sci 2015;8(8):2471–9. http://dx.doi.org/10.1039/c5ee01485a.
[9] Rispoli N, Vitale F, Califano F, Califano M, Polverino P, Rosen MA, Sorrentino M. Constrained optimal design of a reversible solid oxide cell-based multiple load renewable microgrid. J Energy Storage 2020;31(January):101570. http://dx.doi.org/10.1016/j.est.2020.101570.
[10] Vitale F, Rispoli N, Sorrentino M, Rosen MA, Pianese C. On the use of dynamic programming for optimal energy management of grid-connected reversible solid oxide cell-based renewable microgrids. Energy 2021;225:120304. http://dx.doi.org/10.1016/j.energy.2021.120304.
[11] Califano M, Sorrentino M, Rosen MA, Pianese C. Optimal heat and power management of a reversible solid oxide cell based microgrid for effective technoeconomic hydrogen consumption and storage. Appl Energy 2022;319(April):119268. http://dx.doi.org/10.1016/j.apenergy.2022.119268.
[12] Hutty TD, Dong S, Brown S. Suitability of energy storage with reversible solid oxide cells for microgrid applications. Energy Convers Manage 2020;226(October):113499. http://dx.doi.org/10.1016/j.enconman.2020.113499.
[13] Zong Z, Zhou J, Zhang Z, Zhao H, Wang J, Ma W, Wu K. Dynamic analysis of current overshoots in reversible solid oxide cells. Int J Hydrogen Energy 2021;46(70):34896–911. http://dx.doi.org/10.1016/j.ijhydene.2021.08.048.
[14] Bianchi FR, Bosio B, Conte F, Massucco S, Mosaico G, Natrella G, Saviozzi M. Modelling and optimal management of renewable energy communities using reversible solid oxide cells. Appl Energy 2023;334(December 2022):120657. http://dx.doi.org/10.1016/j.apenergy.2023.120657.
[15] Wang C, Chen M, Liu M, Yan J. Dynamic modeling and parameter analysis study on reversible solid oxide cells during mode switching transient processes. Appl Energy 2020;263(September 2019):114601. http://dx.doi.org/10.1016/j.apenergy.2020.114601.
[16] Liu G, Zhao W, Li Z, Xia Z, Jiang C, Kupecki J, Pang S, Deng Z, Li X. Modeling and control-oriented thermal safety analysis for mode switching process of reversible solid oxide cell system. Energy Convers Manage 2022;255(December 2021). http://dx.doi.org/10.1016/j.enconman.2022.115318.
[17] Xiao G, Sun A, Liu H, Ni M, Xu H. Thermal management of reversible solid oxide cells in the dynamic mode switching. Appl Energy 2023;331(June 2022):120383. http://dx.doi.org/10.1016/j.apenergy.2022.120383.
[18] Liu G, Kupecki J, Deng Z, Li X. Efficiency analysis of a novel reversible solid oxide cell system with the secondary utilization of the stack off-gas: A model-based study. J Clean Prod 2023;397(January). http://dx.doi.org/10.1016/j.jclepro.2023.136570.
[19] Aicart J, Di Iorio S, Petitjean M, Giroud P, Palcoux G, Mougin J. Transition cycles during operation of a reversible solid oxide electrolyzer/fuel cell (rSOC) system. Fuel Cells 2019;19(4):381–8. http://dx.doi.org/10.1002/fuce.201800183.
[20] del Pozo Gonzalez H, Bernadet L, Torrell M, Bianchi FD, Tarancón A, Gomis-Bellmunt O, Dominguez-Garcia JL. Power transition cycles of reversible solid oxide cells and its impacts on microgrids. Appl Energy 2023;352:121887. http://dx.doi.org/10.1016/j.apenergy.2023.121887.
[21] Penchini D, Cinti G, Discepoli G, Desideri U. Theoretical study and performance evaluation of hydrogen production by 200 W solid oxide electrolyzer stack. Int J Hydrogen Energy 2014;39(17):9457–66. http://dx.doi.org/10.1016/j.ijhydene.2014.04.052.
[22] Ren J, Gamble SR, Roscoe AJ, Irvine JT, Burt G. Modeling a reversible solid oxide fuel cell as a storage device within ac power networks. Fuel Cells 2012;12(5):773–86. http://dx.doi.org/10.1002/fuce.201100185.
[23] Bujalski W, Dikwal CM, Kendall K. Cycling of three solid oxide fuel cell types. J Power Sources 2007;171(1):96–100. http://dx.doi.org/10.1016/j.jpowsour.2007.01.029.
[24] Gurobi optimizer reference manual. Gurobi Optimization, LLC; 2021.
[25] Beale EML, Tomlin JA. Special facilities in a general mathematical programming system for non-convex problems using ordered sets of variables. OR 1970;69(447–454):99.
[26] D'Ambrosio C, Lodi A, Martello S. Piecewise linear approximation of functions of two variables in MILP models. Oper Res Lett 2010;38(1):39–46. http://dx.doi.org/10.1016/j.orl.2009.09.005.
[27] Bloomberg NEF. Hydrogen economy outlook. Bloomberg New Energy Finance; 2020, p. 12, URL https://data.bloomberglp.com/professional/sites/24/BNEF-Hydrogen-Economy-Outlook-Key-Messages-30-Mar-2020.pdf.
[28] Vartiainen E, Breyer C, Moser D, Román Medina E, Busto C, Masson G, Bosch E, Jäger-Waldau A. True cost of solar hydrogen. Solar RRL 2022;6(5). http://dx.doi.org/10.1002/solr.202100487.